Nano Research
2022, 15(2): 1269–1275

ISSN 1998-0124 CN 11-5974/O4
https://doi.org/10.1007/s12274-021-3645-z

Research Article

Ligand-controlled synthesis of high density and ultra-small Ru nanoparticles with excellent electrocatalytic hydrogen evolution performance

Zhiwen Che[§], Xuyun Lu[§], Bingfeng Cai, Xiangxing Xu, Jianchun Bao, and Ying Liu (✉)

School of Chemistry and Materials Science, Nanjing Normal University, Nanjing 210023, China
[§] Zhiwen Che and Xuyun Lu contributed equally to this work.

Received: 25 March y2021 / **Revised:** 23 May 2021 / **Accepted:** 2 June 2021

ABSTRACT

Ultra-small size metal nanoparticles (u-MNPs) have broad applications in the fields of catalysis, biomedicine and energy conversion. Herein, by means of a ligand-controlled synthesis strategy, series of Ru-based NPs with high dispersity and ultra-small size (marked as u-Ru/C), or sparse and aggregated state (marked as a-Ru/C) anchored on the surface of hollow porous carbon shells are prepared. Systematical *in-situ* thermogravimetry-mass spectrometry-Fourier transform infrared spectra tests suggest that the different ligands in these Ru-based precursors can regulate the nucleation, growth and fixation of metal sites during the pyrolysis process, thus contributing to Ru NPs with various size and dispersity. As a result, when applied to hydrogen evolution reaction, the u-Ru-1/C catalyst displays a low Tafel slope of 26 mV·dec^{-1}, overpotential of 31 mV (at 10 mA·cm^{-2}) and a large exchange current density of 1.7 mA·cm^{-2} in 1.0 M KOH, significantly better than that of the a-Ru-2/C, hollow carbon and even commercial 20% Pt/C. This is mainly because that the u-Ru-1/C sample owns both smaller particle size, more electrochemical active sites, higher intrinsic activity and optimized surface H adsorption ability than that of the a-Ru-2/C counterpart. Such ligand-modulated growth strategy is not only applicable to Ru, but also can be extended to other similar metals, offering a step forward in the design and synthesis of highly dispersed u-MNPs.

KEYWORDS

ultra-small Ru nanoparticles, ligand, *in-situ* test, formation mechanism, hydrogen evolution reaction

1 Introduction

Due to unique optical, electronic and catalytic properties, ultra-small size metal nanoparticles (u-MNPs) have received broad applications in the fields of catalysis, biomedicine and energy conversion [1–3]. The catalytical behaviors of u-MNPs are highly related to their size and dispersity [4, 5]. Generally, the smaller size of the nanoparticles (NPs) and the higher dispersity, the more low-coordinated surface atoms and active sites can be exposed. These atoms and sites will improve the kinetics and yields of diverse electrocatalytic or organic-catalytic reactions [6, 7]. To achieve the fine control of the size and dispersion of MNPs, a variety of synthetic strategies including dipping/impregnation, cluster-nuclei coassemble, molecules-confined pyrolysis and colloidal methods have been designed [8–13]. For example, with Zn-ethylimidazole (MAF-6) as the confined template and tungsten carboxylate as the guest molecule, Li and Zhang's groups have successfully synthesized ultrafine tungsten carbide (WC) NPs (~ 2 nm) through pyrolysis [14]. When applied to electrocatalytic hydrogen evolution reaction (HER), these WC NPs demonstrate excellent HER catalytic activity with an overpotential of 51 mV at 10 mA·cm^{-2} and a Tafel slope of 49 mV·dec^{-1}, as well as good stability and anti-aggregation property. Qiu and Zhang's groups have prepared a variety of narrow-size distributed MNPs (Pd, Pt, Au, PdAu) with triphenylphosphine covalent organic framework (COF) as the carrier [15]. These MNPs (< 2 nm) have shown great catalytic activity, stability and reusability for the Suzuki-Miyaura coupling reaction, the reduction of nitrophenol and 1-bromine 4-nitrobenzene, and the coupling of para-iodine nitrobenzene.

In addition to spatial confinement and carrier anchoring strategies, the coordination of organic or inorganic molecular can isolate adjacent metal ions or atoms spatially, modify their configuration during the nucleation and growth, thus realizing size and dispersion regulation of nanomaterial. For instance, Li's group has synthesized Fe-DNA nanospheres, and realizes the precise control of their size and component via the coordination of Fe(II) and DNA [16]. Besides, through the coordination and self-assembly of metal ions and organic ligands, Liu and Zhang's groups have prepared transition metal phosphide@nitrogen/phosphorus co-doped carbon quasi-aerogel (TMP@NPCA); under the pyrolysis process, organic ligands were carbonized to form the nitrogen/phosphorus co-doped carbon quasi-aerogel framework, while the metal ions were phosphated to transition metal phosphates NPs and anchored onto the three-dimensional (3D) NPCA framework [17]. However, these TMP NPs are still in large size and low dispersity. This could be caused by the poor thermal stability of the ligands in the metal precursor coordination complexes since the rapid decomposition of ligands would lead to naked

Address correspondence to liuyingg@njnu.edu.cn

or coordination-unsaturated metal centers with high surface energy which are unstable and easily self-aggregation. In this case, MNPs with large size and gathered state are usually obtained. In contrast, u-MNPs may be obtained when coordination complexes with high thermal stability are adopted. Nevertheless, to our knowledge, there are few reports on the formation mechanism of thermal decomposition synthesis of u-MNPs, which is likely to facilitate the development of new approaches to advanced metal catalysts.

In this work, by rational selection of different types of Ru-based precursors, Ru-based NPs with different morphological features (including size and dispersity) anchored onto the surface of hollow porous carbon shell are synthesized and related formation mechanism is studied. When cis-bis-(2,2'-bipyridine) dichlororuthenium(II) (denoted as Ru-1) and dichloro (pentametaylcyclopentadienyl) ruthenium(III) polymer (denoted as Ru-3) were used as the precursor, highly dispersed ultrafine Ru NPs (denoted as u-Ru-1/C and u-Ru-3/C, respectively) with a mean size of ~ 1.5 or ~ 2.6 nm were obtained; when tris(2,2'-bipyridine) dichloro ruthenium(II) (denoted as Ru-2) and ruthenium(III) acetylacetonate (denoted as Ru-4) were adopted, sparse and agglomerated Ru NPs (denoted as a-Ru-2/C and a-Ru-4/C, respectively) were attained. Systematical *in-situ* thermogravimetry-mass spectrometry-Fourier transform infrared spectra (TG-MS-FTIR) tests suggest that the different ligands in these Ru-based precursors are responsible for above otherness because ligands can influence the decomposition temperature of corresponding Ru-based precursors, thus regulating the nucleation, growth and fixation of metal sites during the pyrolysis process, and finally contributing to Ru NPs with different size and dispersity. When applied to HER, the u-Ru-1/C catalyst displays a low Tafel slope of 26 mV·dec^{-1}, overpotential of 31 mV (at 10 mA·cm^{-2}, η_{10}) and a large exchange current density (j_0) of 1.7 mA·cm^{-2} in 1.0 M KOH, significantly better than that of the a-Ru-2/C, hollow carbon (HC) and even commercial 20% Pt/C. Such superiority should result from the smaller particle size, more electrochemical active sites, higher intrinsic activity and optimized surface H_{ads} adsorption of the u-Ru-1/C catalyst than those of the a-Ru-2/C and HC counterparts.

2 Experimental

2.1 Chemicals

The 20% Pt/C powder and 5 wt.% Nafion were purchased from Alfa Aesar Chemicals Co. Ltd.. Dichloro (pentametaylcyclopentadienyl) ruthenium(III) polymer and ruthenium(III) acetylacetonate were got from Sigma-Aldrich. Cis-bis-(2,2'-bipyridine) dichloro ruthenium(II) dihydrate, tris(2,2'-bipyridine) dichloro ruthenium(II) hexahydrate, 2,2'-dipyridine, N,N-dimethylformamide, tetraethoxysilane, ammonia (25 wt.%–28 wt.%), sodium chloride, sodium hydroxide, potassium hydroxide, acetone and anhydrous ethanol were bought from Sinopharm Chemical Reagent Co. Ltd.. Poly (diallyldimethylammonium chloride) (PDDA, *M*w < 100,000 Da) and poly (sodium 4-styrenesulfonate) (PSS, *M*w < 70,000 Da) were purchased from Aladdin Industrial Corporation. Ultrapure water used in this work was obtained from a Millipore water purification system (≥ 18.25 MΩ·cm, Millipore SAS Corporation, France). Unless otherwise stated, all the above chemicals were used as received without further purification.

2.2 Characterizations

Transmission electron microscopy (TEM) and high-resolution transmission electron microscopy (HRTEM) images were acquired using a JEOL-2100F apparatus at an accelerating voltage of 200 kV. The scanning transmission electron microscopy (STEM) characterization was performed using an ARM-200CF (JEOL, Tokyo, Japan), transmission electron microscope operated at 200 keV and equipped with double spherical aberration (Cs) correctors. The attainable resolution of the probe defined by the objective pre-field is 78 pm. Powder X-ray diffraction (PXRD) pattern was recorded using a D/max 2500VL/PC diffractometer (Japan) equipped with graphite-monochromatized Cu Kα radiation (λ = 0.154060 nm), and the corresponding scan range, 2θ, was 10° to 90°. X-ray photoelectron spectroscopy (XPS) was conducted using a scanning X-ray microprobe (PHI 5000 Verasa, ULAC-PHI, Inc.) with Al Kα radiation. The hydrocarbon C 1s line at 284.8 eV from adventitious carbon was used as reference for calibrating the binding energy. Thermogravimetry-mass spectromery-Fourier transform infrared spectra (TG-MS-FTIR) tests were conducted using the TG-MS- FTIR system including STA-MS (STA409PC & OMS403C, Netzsch Co. Ltd., Germany) and TG-FTIR (Nicolet iZ10, Thermo Scientific Co. Ltd., USA). Related thermal decomposition conditions are consistent with the annealing conditions in the preparation of the u-Ru/C and a-Ru/C samples. Fourier transform infrared (FT-IR) spectra were taken by Tensor 27 (Bruker, German) in the range of 400–4,000 cm^{-1}.

2.3 Synthesis of catalysts

2.3.1 *Synthesis of m-SiO_2 nanospheres*

For the preparation of m-SiO_2, SiO_2 nanospheres with an average diameter of ~ 388 nm were firstly synthesized according to the modified stöber method. Then the SiO_2 nanospheres (0.2 g) were dispersed in NaCl solution (100 mL, 0.5 M) by sonication for 0.5 h, followed by the addition of PDDA (3.75 g). The suspension was kept stirring for 1 h. Next, the product was washed and centrifugated with ultrapure water to obtain the PDDA-modified SiO_2 nanospheres. Keeping the other experimental conditions unchanged, replacing PDDA with PSS (0.75 g), a layer of PSS was further modified onto the surface of above PDDA-modified SiO_2, and PDDA/PSS-modified SiO_2 nanospheres would be obtained. By repeating the similar process, layers of PDDA and PSS were further coated onto the surface of above PDDA/PSS-modified SiO_2 nanospheres, harvesting the PDDA/PSS/PDDA/PSS-modified SiO_2 nanospheres (i.e., m-SiO_2).

2.3.2 *Synthesis of u-Ru/C, a-Ru/C and HC*

The u-Ru/C sample was synthesized in three steps: firstly, 40 mg of m-SiO_2 was dispersed in 10 mL water with the assistance of ultrasonic. Then cis-bis-(2,2'-bipyridine) dichlororuthenium(II) dihydrate (denoted as Ru-1) (40.0 mg, 76.9 mmol) was added to the above m-SiO_2 suspension and stirred for 30 min. After that, the suspension was centrifuged and separated to give the m-SiO_2@Ru-1 intermediate (atropurpureus solid). Thereafter, the m-SiO_2@Ru-1 power was annealed at 800 °C and maintained at this temperature for 1 h under Ar atmosphere. After naturally cooled to room temperature, the powder was dissolved in 20 mL NaOH (1 M) and etched treatment by a hydrothermal method at 80 °C for 12 h. Finally, the suspension was centrifuged and separated to harvest the u-Ru-1/C product.

Keeping the other experimental conditions constant, replacing Ru-1 with Ru-3 (23.6 mg, 76.9 mmol), m-SiO_2@Ru-3 intermediate (black solid) and u-Ru-3/C product with ultrafine size and high dispersity would be obtained. Differently, when Ru-2 (57.5 mg, 76.9 mmol) or Ru-4 (30.6 mg, 76.9 mmol) was adopted as the Ru-based precursor, m-SiO_2@Ru-2 (orange-yellow

solid) or m-SiO_2@Ru-4 (red solid) intermediate, and a-Ru-2/C and a-Ru-4/C products with large size and aggregated state would be obtained. Considering the differences of adsorption/solubility ability of different Ru-based precursors, the surface adsorption of m-SiO_2@Ru-2 was conducted in a mixture of ultrapure water and DMF (volume ratio of 9:1).

As comparison, in the absence of metal salt, we also prepared HC counterpart, and detailed annealing and etching procedures are consistent with that of the u-Ru/C and a-Ru/C samples.

2.4 Electrochemical tests

The electrochemical HER experiments were conducted using a CHI 660D electrochemical workstation with a typical three-electrode cell setup. Graphite rod was used as the counter electrode, while Hg/HgO (1 M KOH) was acted as the reference electrode, and a glassy carbon electrode (GCE) (3 mm in diameter) was served as the working electrode. To prepare the catalyst ink, a certain amount of catalyst were mixed with ethanol and ultrapure water (volume ratio of 1:3) and then ultrasonicated for approximately 30 min to obtain catalyst ink with the same molar amount of Ru. Then, 10 μL of above catalyst ink was pipetted onto the surface of a cleaned GCE and air dried, followed by the coating of 5 μL Nafion solution (1.0 wt.%). All electrochemical measurements were conducted in N_2-saturated 1.0 M KOH solution at room temperature. Prior to each electrochemical test, the modified electrodes were pre-treated by performing several cyclic voltammetry (CV) cycles until the potential was stable to remove any possible surface contamination. The CV tests were conducted using a potential window from –1.2 to –0.8 V (vs. Ag/AgCl), and polarization curves were obtained using a potential window from –1.4 to –0.8 V (vs. Ag/AgCl) after iR compensation with a scan rate of 2 $mV \cdot s^{-1}$. To evaluate the electrochemical surface area of different catalysts, related CV tests were carried out in the non-Faraday potential range of the corresponding catalyst. All potentials were referenced to reversible hydrogen electrode (RHE) values using the equation E (vs. RHE) = E (vs. Hg/HgO) + 0.098 + 0.059pH = E (vs. Hg/HgO) + 0.924.

3 Results and discussion

3.1 Morphology and microstructure characterization

Figure 1 shows the morphology and microstructure features of the u-Ru-1/C and a-Ru-2/C samples. From the STEM images in Figs. 1(a)–1(c), ultra-thin hollow carbon shells with highly-dispersed ultrafine Ru NPs anchored on their surface were observed. These NPs were measured to be about 1.5 nm in diameter (Fig. 1(d)), equaling to the size of ~ 140 close-packed Ru atoms. Figure 1(e) shows the high-resolution TEM image of the NPs, and obvious lattice fringes with a spacing of 0.23 nm are observed, matching well with the (100) crystal plane of hexagonal Ru (JCPDS 65–1863). Figure 1(f) displays the PXRD pattern of the u-Ru-1/C sample, and no obvious diffraction peaks are detected, which should result from the ultra-small size of Ru NPs [18]. Figure S1 in the Electronic Supplementary Material (ESM) shows the N_2 adsorption-desorption curve of the u-Ru-1/C sample, from which a typical type-IV adsorption isotherm with obvious hysteresis is observed, indicating a porous structure. The measured pore size is in the range of 1.5–3 nm, which will facilitate mass transfer and gas diffusion under electro-catalytic process. Figures 1(g)–1(i) depict the TEM and size distribution diagrams of the a-Ru-2/C sample, and aggregated NPs with messy state are observed. Related HRTEM image in Fig. S2(a) in the ESM also displays a lattice fringes spacing of 0.23 nm while the XRD pattern (Fig. S2(b) in the ESM) shows weak Ru diffraction peaks. These results are in good according with

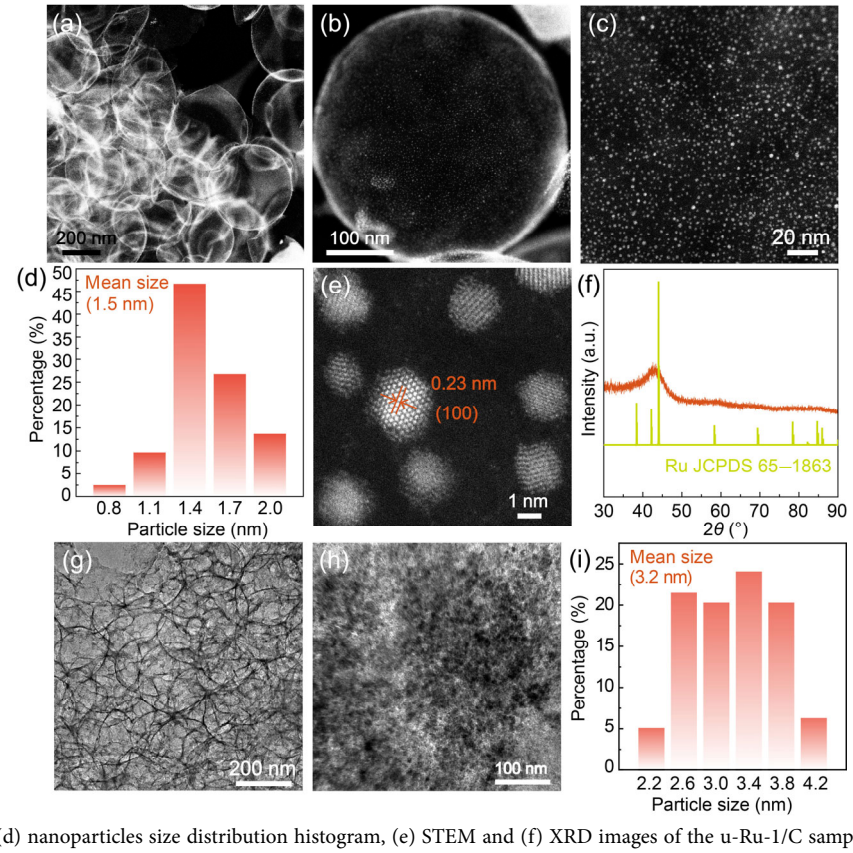

Figure 1 (a)–(c) STEM, (d) nanoparticles size distribution histogram, (e) STEM and (f) XRD images of the u-Ru-1/C sample. (g) and (h) TEM and (i) nanoparticles size distribution histogram of the a-Ru-2/C sample.

the features of hexagonal Ru (JCPDS 65–1863), certifying an a-Ru-2/C construction.

3.2 Synthesis process and formation mechanism investigation

Scheme 1 illustrates the synthesis process of the u-Ru-1/C and a-Ru-2/C samples, which mainly includes three steps: (1) fabrication of m-SiO_2@Ru precursors using a dipping method; (2) high temperature annealing treatment to convert the m-SiO_2@Ru precursors to m-SiO_2@Ru/C intermediates; (3) etching treatment to remove the SiO_2 templates and harvest the u-Ru-1/C and a-Ru-2/C products. Specifically, m-SiO_2 nanospheres with a certain thickness of PDDA and PSS polymers coated on their surface were firstly synthesized based on a reported method with some modification (Fig. S3 in the ESM) [19, 20]. Then m-SiO_2@Ru precursors were fabricated by means of dipping of different Ru-based precursors onto the surface of above m-SiO_2 nanospheres. When facing with the subsequent high temperature annealing treatment, the PDDA and PSS polymers were decomposed to form the ultrathin carbon layer. Simultaneously, the Ru-based precursor was reduced and grown into Ru nanocluster/NPs gradually [21] (Fig. S4 in the ESM). Considering that the morphological differences of the resultant Ru NPs are mainly derived from different Ru-based precursors, we performed *in-situ* TG-MS-FTIR tests on the Ru-1 and Ru-2 precursors. As shown in Fig. 2(a), it was observed that when the heat treatment temperature increased gradually from room temperature to ~ 133 °C, ~ 8.6% weight loss was observed for the Ru-1 precursor; meanwhile, MS analysis detected a large quantities of ions with nucleus-to-mass ratio (*m*/*z*) of 17 and 18 which should originate from water molecules (Fig. 2(b)) [22]. These results indicate that the weight loss at this temperature is mainly caused by the removal of crystal water and other surface adsorbates. When heating up to ~ 400 °C, no obvious weight loss was detected, suggesting that the Ru-1 precursor was relatively thermally stable at this stage. When the temperature exceeds 401 °C, another ~ 7.8% weight loss was obtained, and large number of ions with *m*/*z* of 35 was detected (Fig. 2(c)) which could be ascribed to the removal of Cl ions. This was further demonstrated by the infrared (IR) spectra in Figs. 2(e) and 2(f), where obvious signal of chlorinated hydrocarbon groups (wavenumber < 1,000 cm^{-1}) was observed. The Ru-N bonds (nitrogen from bipyridine) in Ru-1 precursor began to break when the temperature rises to 506 °C, accompanying the decomposition of bipyridine and release of -CN species as confirmed by the MS and IR analyses [23] (Figs. 2(d) and 2(f)). When the temperature reaches to 900 °C, the mass of the Ru-1 precursor is basically stable and the final remaining weight percentage is ~ 62.4%. This value is significantly larger than the mass percentage of Ru in the Ru-1 precursor (19.4%), suggesting that part of the bipyridines should have been transformed into carbon layer. TEM image of the product obtained from the direct pyrolysis of Ru-1 precursor confirms this transformation (Fig. S5 in the ESM). As for the Ru-2 precursor, it began to decompose at 366 °C and lose one of the three bipyridine ligand (corresponding to the ions with *m*/*z* of 79 in MS spectrum and the absorption peak at 1,500 cm^{-1} in IR profile) (Figs. S6 and S7 in the ESM). This will lead to coordination unsaturated Ru-2 molecules which tend to migrate and aggregate to form Ru NPs with large size and poor dispersity due to high surface energy under subsequent thermal treatment process (Fig. S6(f) in the ESM). These results indicate that the marked morphological differences of

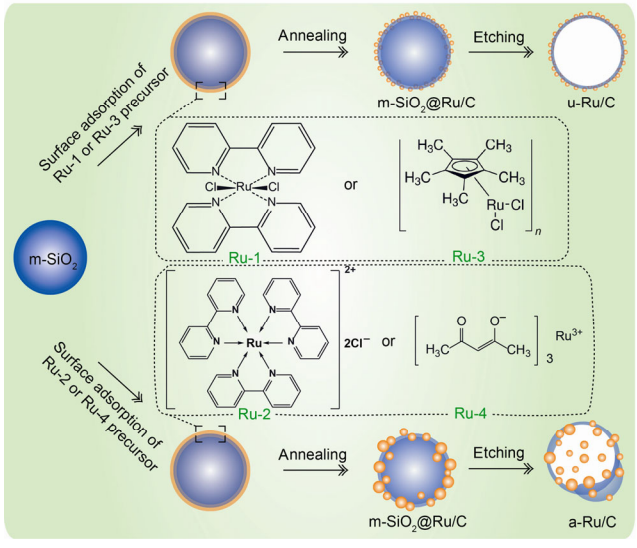

Scheme 1 Schematic illustration of the controllable synthesis of u-Ru/C and a-Ru/C.

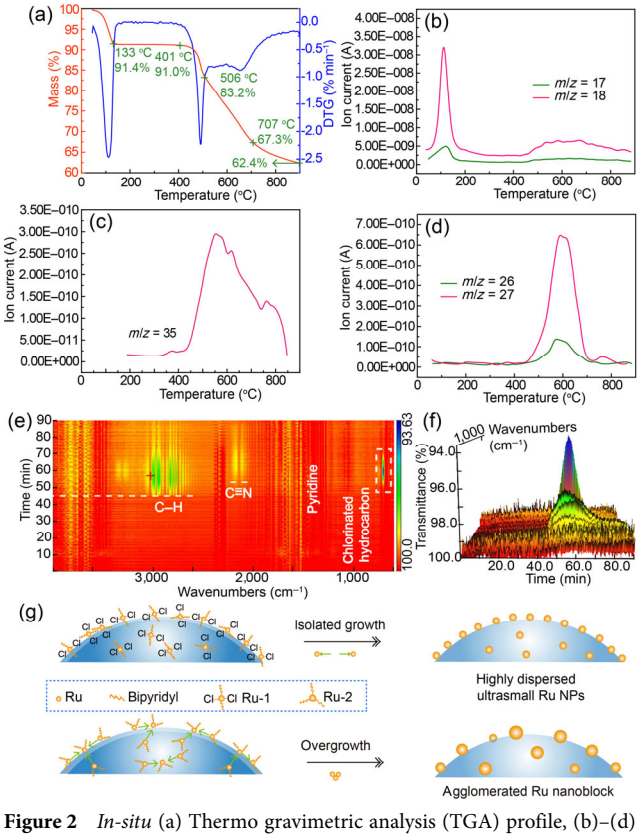

Figure 2 *In-situ* (a) Thermo gravimetric analysis (TGA) profile, (b)–(d) MS and (e) and (f) FT-IR spectra of the Ru-1 precursor under pyrolysis process. (g) Schematic illustration of the formation mechanism of the u-Ru-1/C and a-Ru-2/C.

the u-Ru-1/C and a-Ru-2/C samples should result from their differences in initial decompose temperature and ligands, i.e., the initial decompose temperature of Ru-1 precursor is higher than that of the Ru-2 precursor, then under high temperature annealing conditions, the ligands in Ru-1 precursor are more stable and can maintain their coordination state within a certain temperature range, which are not only favorable in isolating the adjacent Ru seeds, but also in anchoring the Ru seeds onto the *in-situ* formed carbon layer and preventing their migration and aggregation effectively, thus finally leading to the formation of highly dispersed ultrafine Ru NPs (Fig. 2(g)).

To verify this ligand-regulated formation mechanism, two other precursors, Ru-3 and Ru-4 were further employed and investigated. As shown in Fig. S8 in the ESM, the Ru-3 precursor shows higher initial decomposition temperature than that of the Ru-4 precursor. Correspondingly, the product obtained from Ru-3 precursor shows more uniform morphology and smaller size than that obtained from the Ru-4 precursor (Fig. S9 in the ESM). Furthermore, the thermal decomposition temperature of Ru-4 is the lowest among these four Ru-based precursors, and the size of the Ru NPs obtained from Ru-4 precursor is also the largest. These results are consistent with above ligand-regulated formation mechanism, which is of great significance for the design and controllable synthesis of u-MNPs.

In addition, zeta potential and FT-IR tests showed that the different Ru-based precursors had different affinity to the m-SiO_2 nanospheres. As shown in Fig. S10 in the ESM, the m-SiO_2 presents a zeta potential of –53 mV, while the m-SiO_2@Ru-1 and m-SiO_2@Ru-2 samples display markedly decreasing zeta potentials of –23 and –30 mV, respectively, indicating that there is strong electrostatic interaction between the m-SiO_2 and Ru-based precursors. And importantly, the electrostatic interaction between the m-SiO_2 and Ru-1 precursor is stronger than that between the m-SiO_2 and Ru-2 precursor. As a result, when Ru-1 precursor was adsorbed, the obtained m-SiO_2@Ru-1 sample shows obvious characteristic absorption peaks related to the C–H and C=N, while the adsorption of Ru-2 precursor results in similar FT-IR absorption peaks but weaker peak intensity (Fig. S11 in the ESM). This will cause the surface adsorption of more Ru-1 precursor onto the surface of m-SiO_2 nanospheres, leading to the easily formation of large-sized NPs. Nevertheless, the resultant u-Ru-1/C product still demonstrates smaller size and better dispersity than that of the a-Ru-2/C product, further confirming that ligands can regulate the nucleation and growth of MNPs. This not only helps to reduce the size of Ru NPs, but also may be assistant in improving the electrocatalytic performances.

3.3 Electrocatalytic HER performances

The electrocatalytic HER performances of the u-Ru-1/C, a-Ru-2/C, HC (Fig. S12 in the ESM) and commercial 20% Pt/C catalysts are subsequently investigated in N_2-saturated 1.0 M KOH. Figure 3(a) shows the polarization curves of these catalysts, from which obvious increase in activity (based on onset potential) is observed in the following order: HC < a-Ru-2/C < 20% Pt/C < u-Ru-1/C. To further evaluate the reaction kinetics differences of these catalysts, their Tafel slopes are fitted according to the polarization curves. As shown in Fig. 3(b), the u-Ru-1/C catalyst displays a small Tafel slope of 26 mV·dec^{-1}, superior to the a-Ru-2/C (36 mV·dec^{-1}), HC (307 mV·dec^{-1}) and commercial 20% Pt/C (32 mV·dec^{-1}), indicating a two-electron transfer process following the Volmer-Heyrovsky mechanism and faster reaction kinetics for the u-Ru-1/C catalyst [24]. Besides, the u-Ru-1/C catalyst also demonstrates smaller overpotential at 10 mA·cm^{-2} (η_{10}, 31 mV) than that of the a-Ru-2/C (172 mV) and 20% Pt/C (51 mV) catalysts; and the j_0 value of the u-Ru-1/C catalyst (1.7 mA·cm^{-2}) is 8.5 times higher than that of the a-Ru-2/C counterpart (0.2 mA·cm^{-2}) (Fig. 3(c)). These performances outperform many recently reported catalysts, further proving the excellent HER catalytic properties of the u-Ru-1/C catalyst (Table S2 in the ESM). In addition to activity, stability is another important parameter to assess the application prospects of different catalysts, so the electrocatalytic stability of the u-Ru-1/C catalyst is further tested. As shown in Fig. 3(d), no obvious

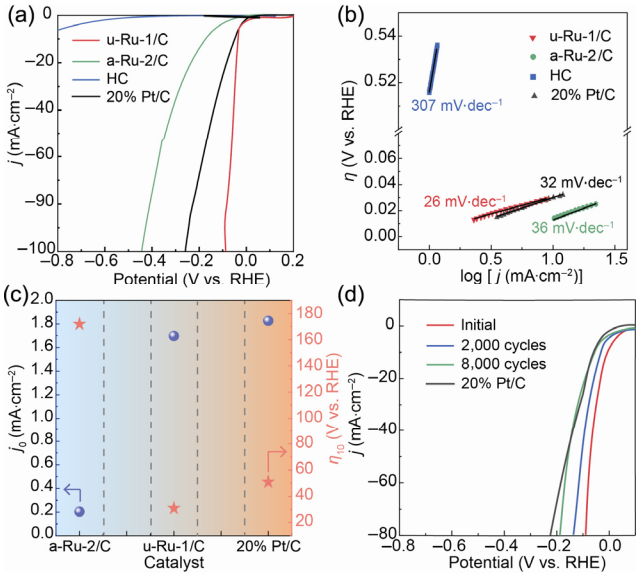

Figure 3 (a) HER polarization curves for the u-Ru-1/C, a-Ru-2/C, HC, and commercial 20% Pt/C catalysts. Comparisons of (b) Tafel plots (c) j_0, and η_{10} values of different catalysts. (d) Stability tests of the u-Ru-1/C catalyst.

decay in both onset potential and current density are observed for the u-Ru-1/C catalyst after 2,000 cycles; when the test continues to 8,000 cycles, a certain degree of attenuation is observed, but the obtained electro-catalytic activity still better than that of the commercial 20% Pt/C. Further time-dependent galvanostatic measurement also displays relatively stable current under 10 h continues test, indicating the goodish catalytic stability of the u-Ru-1/C catalyst (Fig. S13 in the ESM). Figure S14 in the ESM shows the XRD, TEM, HRTEM and XPS images of the u-Ru-1/C catalyst after stability test, and it was observed that although the size of the Ru nanoparticles after stability test became slightly larger, related morphology and microstructural features were basically preserved, indicative of its decent chemical and structural stability.

3.4 Origin of the electrocatalytic HER performances

To further learn the reasons for the different HER catalytic activity of the u-Ru-1/C and a-Ru-2/C catalysts, we conducted X-ray photoelectron spectra and electrochemical impedance tests. For comparison, we have prepared pure Ru nanoparticles (without carbon) before XPS tests. Figure 4(a) shows the XPS spectra of the u-Ru-1/C, a-Ru-2/C and pure Ru catalysts, and it was observed that although the u-Ru-1/C and a-Ru-2/C catalysts display similar Ru 3p fine XPS spectra, their binding energies are both higher than that of the pure Ru nanoparticles, indicating that there is strong electronic interaction between the Ru nanoparticles and the HC shell, and the electron should transfer from Ru to HC shell [25]. According to the literature, the surface adsorption energy of metallic Ru to H_{ads} is a little bit stronger, then this transfer will relieve and optimize the adsorption of Ru to H_{ads} and thus improve their reaction kinetics [26]. As for the N 1s fine spectrum (Fig. 4(b)), the u-Ru-1/C catalyst displays two deconvoluted peaks corresponding to pyridinic N (398.4 eV) and graphitic N (400.3 eV), respectively, and the a-Ru-2/C catalyst shows three deconvoluted peaks related to pyridinic N, graphitic N and oxidized N (403.5 eV), respectively [27]. The pyridinic N (17.7%) and graphitic N (82.3%) contents in u-Ru-1/C are higher than those of the a-Ru-2/C (11.0% pyridinic N and 81.2% graphitic N) based on the integration calculation of their peak area. Considering that pyridinic N is electroactive

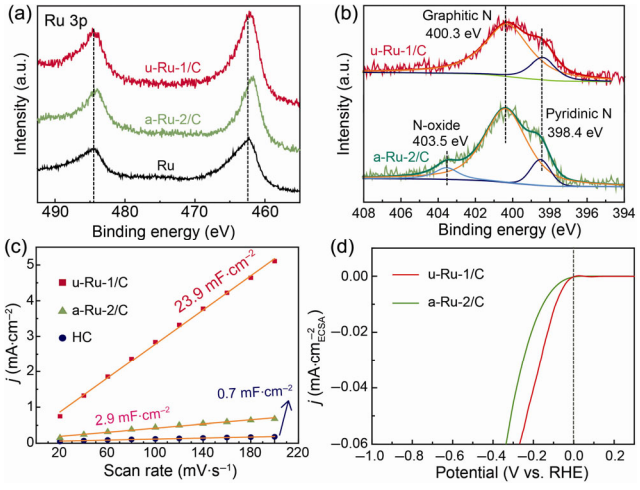

Figure 4 (a) Ru 3p fine XPS spectra for the u-Ru-1/C, a-Ru-2/C and pure Ru catalysts. (b) N 1s fine XPS spectra for the u-Ru-1/C and a-Ru-2/C catalysts. (c) C_{dl} and (d) normalized HER polarization curves of different catalysts.

in HER, and graphitic N can improve electron transfer [28], the higher concentrations of these two N species will boost the electrocatalytic activity of the u-Ru-1/C catalyst. Moreover, electrochemical impedance tests show that the interface electron transfer resistance of the u-Ru-1/C sample (37 Ω) was significantly smaller than that of the a-Ru-2/C (120 Ω) and HC samples based on the fitted circuit in the inset (Fig. S15 in the ESM), indicating that the u-Ru-1/C catalyst has faster electron transfer efficiency than that of the a-Ru-2/C and HC. Besides, the u-Ru-1/C catalyst still demonstrates greater electrochemical double layer capacitance (C_{dl}) value (23.9 mF·cm^{-2}) than that of the a-Ru-2/C (2.9 mF·cm^{-2}) and HC (0.7 mF·cm^{-2}) (Fig. 4(c) and Fig. S16 in the ESM) counterparts, signifying that the u-Ru-1/C catalyst has more electrochemical active sites. To assess the activity of Ru in different catalysts and eliminate the influence of carbon on the total electrochemical surface area (ECSA), the C_{dl} values after deducting the C_{dl} value of HC were adopted to calculate the ECSA of different catalysts. As shown in Fig. S17 in the ESM, the u-Ru-1/C catalyst demonstrates larger ECSA value than that of the a-Ru-2/C catalyst, which should originate from its smaller size and high dispersity. To further exclude the effect of ECSA on the electrocatalytic activity, the polarization curves in Fig. 3(a) were normalized by ECSA. As shown in Fig. 4(d), the u-Ru-1/C catalyst still exhibits smaller onset potential and larger current density than that of the a-Ru-2/C and HC catalysts, indicating the excellent intrinsic activity of the u-Ru-1/C catalyst.

4 Conclusions

In summary, this work develops an artful ligand tactics for the construction of highly-dispersed ultra-small Ru NPs (~ 1.5 nm) through delicate controlling the nucleation and growth of Ru seeds. By means of *in-situ* MS-IR analyses, the decomposition process of different Ru-based precursors and formation mechanism of the u-Ru-1/C and a-Ru-2/C samples were investigated, which is beneficial to understand the factors affecting the growth of nanocrystals. Compared with the a-Ru-2/C and HC counterparts, the u-Ru-1/C catalyst exhibits both more electrochemical active sites, higher intrinsic activity, optimized surface H_{ads} adsorption energy, and significantly enhanced HER catalytic performances. This ligand-regulated synthesis strategy is not only applicable to Ru, but also can be extended to other similar metals or compounds, thus representing an innovation strategy for the development of ultrafine NPs or nanoclusters.

Acknowledgements

This work was supported by the National Natural Science Foundation of China (Nos. 22075147 and 21533012), the PAPD of Jiangsu Higher Education Institutions.

Electronic Supplementary Material: Supplementary material (material characterization by means of Brunner-Emmet-Teller (BET), TEM, HRTEM, *in-situ* TG-MS-FTIR, XRD, FT-IR and electrochemical CV curves, as well as the comparison of electrocatalytic HER performances with some recently reported catalysts) is available in the online version of this article at http://doi.org/10.1007/s12274-021-3645-z.

References

[1] Chen, P. C.; Liu, Y.; Du, J. S.; Meckes, B.; Dravid, V. P.; Mirkin, C. A. Chain-end functionalized polymers for the controlled synthesis of sub-2 nm particles. *J. Am. Chem. Soc.* **2020**, *142*, 7350–7355.

[2] Li, R.; Linares, N.; Sutjianto, J. G.; Chawla, A.; Garcia-Martinez, J.; Rimer, J. D. Ultrasmall zeolite l crystals prepared from highly interdispersed alkali-silicate precursors. *Angew. Chem., Int. Ed.* **2018**, *57*, 11283–11288.

[3] Li, X.; Lu, Z. L.; Wang, T. Self-assembly of semiconductor nanoparticles toward emergent behaviors on fluorescence. *Nano Res.* **2021**, *14*, 1233–1243.

[4] Huang, Y.; Song, X. N.; Deng, J.; Zha, C.; Huang, W. J.; Wu, Y. L.; Li, Y. G. Ultra-dispersed molybdenum phosphide and phosphosulfide nanoparticles on hierarchical carbonaceous scaffolds for hydrogen evolution electrocatalysis. *Appl. Catal. B Environ.* **2019**, *245*, 656–661.

[5] Xu, S. L.; Shen, S. C.; Wei, Z. Y.; Zhao, S.; Zuo, L. J.; Chen, M. X.; Wang, L.; Ding, Y. W.; Chen, P.; Chu, S. Q. et al. A library of carbon-supported ultrasmall bimetallic nanoparticles. *Nano Res.* **2020**, *13*, 2735–2740.

[6] Sun, T. T.; Li, Y. L.; Cui, T. T.; Xu, L. B.; Wang, Y. G.; Chen, W. X.; Zhang, P. P.; Zheng, T. Y.; Fu, X. Z.; Zhang, S. L. et al. Engineering of coordination environment and multiscale structure in single-site copper catalyst for superior electrocatalytic oxygen reduction. *Nano Lett.* **2020**, *20*, 6206–6214.

[7] Cao, S. W.; Tao, F.; Tang, Y.; Li, Y. T.; Yu, J. G. Size- and shape-dependent catalytic performances of oxidation and reduction reactions on nanocatalysts. *Chem. Soc. Rev.* **2016**, *45*, 4747–4765.

[8] Lu, Y. X.; Dong, C. L.; Huang, Y. C.; Zou, Y. Q.; Liu, Z. J.; Liu, Y. B.; Li, Y. Y.; He, N. H.; Shi, J. Q.; Wang, S. Y. Identifying the geometric site dependence of spinel oxides for the electrooxidation of 5-hydroxymethylfurfural. *Angew. Chem., Int. Ed.* **2020**, *59*, 19215–19221.

[9] Wang, Q.; Ming, M.; Niu, S.; Zhang, Y.; Fan, G. Y.; Hu, J. S. Scalable solid-state synthesis of highly dispersed uncapped metal (Rh, Ru, Ir) nanoparticles for efficient hydrogen evolution. *Adv. Energy Mater.* **2018**, *8*, 1801698.

[10] Yasuda, S.; Osuga, R.; Kunitake, Y.; Kato, K.; Fukuoka, A.; Kobayashi, H.; Gao, M.; Hasegawa, J. Y.; Manabe, R.; Shima, H. et al. Zeolite-supported ultra-small nickel as catalyst for selective oxidation of methane to syngas. *Commun. Chem.* **2020**, *3*, *129*.

[11] Yang, F.; Ye, J. Y.; Yuan, Q.; Yang, X. T.; Xie, Z. X.; Zhao, F. L.; Zhou, Z. Y.; Gu, L.; Wang, X. Ultrasmall Pd–Cu–Pt trimetallic twin icosahedrons boost the electrocatalytic performance of glycerol oxidation at the operating temperature of fuel cells. *Adv. Funct. Mater.* **2020**, *30*, 1908235.

[12] Liu, J. L.; Shi, W. X.; Wang, X. Cluster-nuclei coassembled into two-dimensional hybrid CuO-PMA sub-1 nm nanosheets. *J. Am. Chem. Soc.* **2019**, *141*, 18754–18758.

[13] Yang, Z. K.; Wang, Y.; Zhu, M. Z.; Li, Z. J.; Chen, W. X.; Wei, W. C.; Yuan, T. W.; Qu, Y. T.; Xu, Q.; Zhao, C. M. et al. Boosting oxygen

reduction catalysis with Fe-N_4 sites decorated porous carbons toward fuel cells. *ACS Catal*. **2019**, *9*, 2158–2163.

[14] Xu, Y. T.; Xiao, X. F.; Ye, Z. M.; Zhao, S. L.; Shen, R. A.; He, C. T.; Zhang, J. P.; Li, Y. D.; Chen, X. M. Cage-confinement pyrolysis route to ultrasmall tungsten carbide nanoparticles for efficient electrocatalytic hydrogen evolution. *J. Am. Chem. Soc*. **2017**, *139*, 5285–5288.

[15] Tao, R.; Shen, X. R.; Hu, Y. M.; Kang, K.; Zheng, Y. Q.; Luo, S. C.; Yang, S. Y.; Li, W. L.; Lu, S. L.; Jin, Y. H. et al. Phosphine-based covalent organic framework for the controlled synthesis of broad-scope ultrafine nanoparticles. *Small* **2020**, *16*, 1906005.

[16] Li, M. Y.; Wang, C. L.; Di, Z. H.; Li, H.; Zhang, J. F.; Xue, W. T.; Zhao, M. P.; Zhang, K.; Zhao, Y. L.; Li, L. L. Engineering multifunctional DNA hybrid nanospheres through coordination-driven self-assembly. *Angew. Chem., Int. Ed*. **2019**, *58*, 1350–1354.

[17] Guo, H. L.; Feng, Q. C.; Xu, K. W.; Xu, J. S.; Zhu, J. X.; Zhang, C.; Liu, T. X. Self-templated conversion of metallogel into heterostructured tmp@carbon quasiaerogels boosting bifunctional electrocatalysis. *Adv. Funct. Mater*. **2019**, *29*, 1903660.

[18] Liu, Y.; Liu, S. L.; Wang, Y.; Zhang, Q. H.; Gu, L.; Zhao, S. C.; Xu, D. D.; Li, Y. F.; Bao, J. C.; Dai, Z. H. Ru modulation effects in the synthesis of unique rod-like Ni@Ni_2P-Ru heterostructures and their remarkable electrocatalytic hydrogen evolution performance. *J. Am. Chem. Soc*. **2018**, *140*, 2731–2734.

[19] Zhang, C.; Shi, Y. M.; Yu, Y. F.; Du, Y. H.; Zhang, B. Engineering sulfur defects, atomic thickness, and porous structures into cobalt sulfide nanosheets for efficient electrocatalytic alkaline hydrogen evolution. *ACS Catal*. **2018**, *8*, 8077.

[20] Tang, C. J.; Liu, Y. N.; Xu, C.; Zhu, J. X.; Wei, X. J.; Zhou, L.; He, L.; Yang, W.; Mai, L. Q. Ultrafine nickel-nanoparticle-enabled SiO_2 hierarchical hollow spheres for high-performance lithium storage. *Adv. Funct. Mater*. **2018**, *28*, 1704561.

[21] Mei, J.; Ayoko, G. A.; Hu, C. F.; Sun, Z. Q. Thermal reduction of sulfur-containing MAX phase for MXene production. *Chem. Eng. J*. **2020**, *395*, 125111

[22] Madarász, J.; Bombicz, P.; Okuya, M.; Kaneko, S.; Pokol, G. Online coupled TG-FTIR and TG-/DTA-MS analyses of the evolved gases from dichloro(thiourea) tin(II). *Solid State Ionics* **2004**, *172*, 577–581.

[23] Li, G. Y.; Ma, F. F.; Cao, Q. J. W.; Zheng, Z.; DeLaney, K.; Liu R.; Li, L. J. Nanosecond photochemically promoted click chemistry for enhanced neuropeptide visualization and rapid protein labeling. *Nat. Commun*. **2019**, *10*, 4697.

[24] Niu, S. W.; Cai, J. Y.; Wang, G. M. Two-dimensional MoS_2 for hydrogen evolution reaction catalysis: The electronic structure regulation. *Nano Res*. **2021**, *14*, 1985-2002.

[25] Zhao, D.; Sun, K. A.; Cheong, W. C.; Zheng, L. R.; Zhang, C.; Liu, S. J.; Cao, X.; Wu, K. L.; Pan, Y.; Zhuang, Z. W. et al. Synergistically interactive pyridinic-N-MoP sites: Identified active centers for enhanced hydrogen evolution in alkaline solution. *Angew. Chem., Int. Ed*. **2020**, *59*, 8982–8990.

[26] Ju, Q. J.; Ma, R. G.; Pei, Y.; Guo, B. B.; Li, Z. C.; Liu, Q.; Thomas, T.; Yang, M. H.; Hutchings, G. J.; Wang, J. C. Ruthenium triazine composite: A good match for increasing hydrogen evolution activity through contact electrification. *Adv. Energy Mater*. **2020**, *10*, 2000067.

[27] Lu, L. Z.; Liu, Y.; Fan, J. Y.; Wang, L.; Lin, Y.; Xu, D. D.; Dai, Z. H.; Han, M. Engineering bimetal Cu, Co sites on 3D N-doped porous carbon nanosheets for enhanced oxygen reduction electrocatalysis. *Chem. Commun*. **2020**, *56*, 10010–10013.

[28] Li, F.; Han, G. F.; Noh, H. J.; Jeon, J. P.; Ahmad, I.; Chen, S. S.; Yang, C.; Bu, Y. F.; Fu, Z. P.; Lu, Y. L. et al. Balancing hydrogen adsorption/desorption by orbital modulation for efficient hydrogen evolution catalysis. *Nat. Commun*. **2019**, *10*, 4060.